

Morlet Wavelet Filtering and Phase Analysis to Reduce the Limit of Detection for Thin Film Optical Biosensors

Simon J. Ward, Rabeb Layouni, Sofia Arshavsky-Graham, Ester Segal, and Sharon M. Weiss*

Cite This: *ACS Sens.* 2021, 6, 2967–2978

Read Online

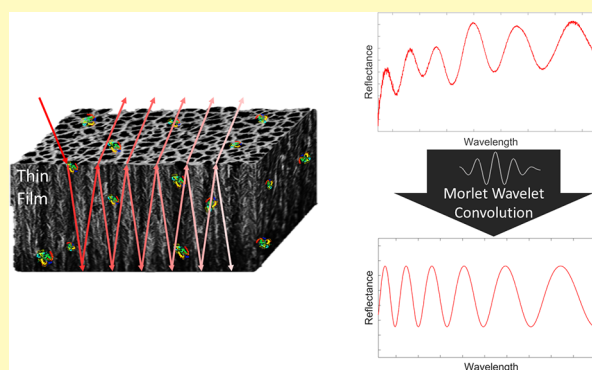
ACCESS |

Metrics & More

Article Recommendations

ABSTRACT: The ultimate detection limit of optical biosensors is often limited by various noise sources, including those introduced by the optical measurement setup. While sophisticated modifications to instrumentation may reduce noise, a simpler approach that can benefit all sensor platforms is the application of signal processing to minimize the deleterious effects of noise. In this work, we show that applying complex Morlet wavelet convolution to Fabry–Pérot interference fringes characteristic of thin film reflectometric biosensors effectively filters out white noise and low-frequency reflectance variations. Subsequent calculation of the average difference in extracted phase between the filtered analyte and reference signals enables a significant reduction in the limit of detection (LOD). This method is applied on experimental data sets of thin film porous silicon sensors (PSi) in buffered solution and complex media obtained from two different laboratories. The demonstrated improvement in the LOD achieved using wavelet convolution and average phase difference paves the way for PSi optical biosensors to operate with clinically relevant detection limits for medical diagnostics, environmental monitoring, and food safety.

KEYWORDS: signal processing, thin film, limit of detection, porous silicon, wavelet noise reduction, label free, aptasensors



Detecting low levels of an analyte is crucial for a wide variety of sensing applications, including medical diagnostics in which early detection of low concentrations of disease biomarkers enables preventative measures and treatments with exponentially higher rates of positive patient outcomes¹ and environmental monitoring in which detection of toxic substances harmful to humans at ultralow levels can save lives.² Of the many ways to improve the limit of detection (LOD), arguably the cheapest and easiest strategy is signal processing, which can improve detection limits by removing various noise signatures. Signal processing for noise reduction is applicable to all systems, from costly, high-resolution, and highly accurate laboratory instruments to compact, simple, and cheap point-of-care devices.

Signal processing has been used in a wide variety of biosensing platforms to enhance noise immunity, achieve lower detection limits, and provide deeper insights into the physical properties of the sensor and the sensing mechanism. For surface plasmon resonance sensors, one of the most prevalent optical biosensing platforms, techniques such as polynomial fitting,³ centroid detection⁴ and tracking⁵ complemented by dynamic baseline algorithms,⁶ linear data analysis,⁷ locally weighted parametric regression,⁸ and the radon transform technique⁹ have been used for higher resolution resonance detection and reduced noise susceptibility. The performance of

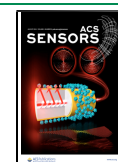
quartz crystal microbalance sensors, another effective and widely used biosensing platform, has also benefitted from signal processing methods, such as the fractional Fourier transform,¹⁰ heterodyning,¹¹ and moving average and Savitzky–Golay filtering.¹² Additionally, frequency locking along with nonlinear filtering has been used to lower the noise floor of microtoroid optical biosensors, enabling single-molecule detection,¹³ and a range of signal processing methods have been applied to measure spectral shifts of guided mode resonant filter biosensors such as cross correlation and maximum likelihood techniques.¹⁴ The most appropriate signal processing approach to utilize depends on the application and the characteristics of the measured signal.

In this work, we introduce a signal processing approach based on Morlet wavelet convolution and phase analysis that can dramatically lower the detection limit of thin film biosensors, which are among the simplest optical biosensor

Received: April 15, 2021

Accepted: July 30, 2021

Published: August 13, 2021



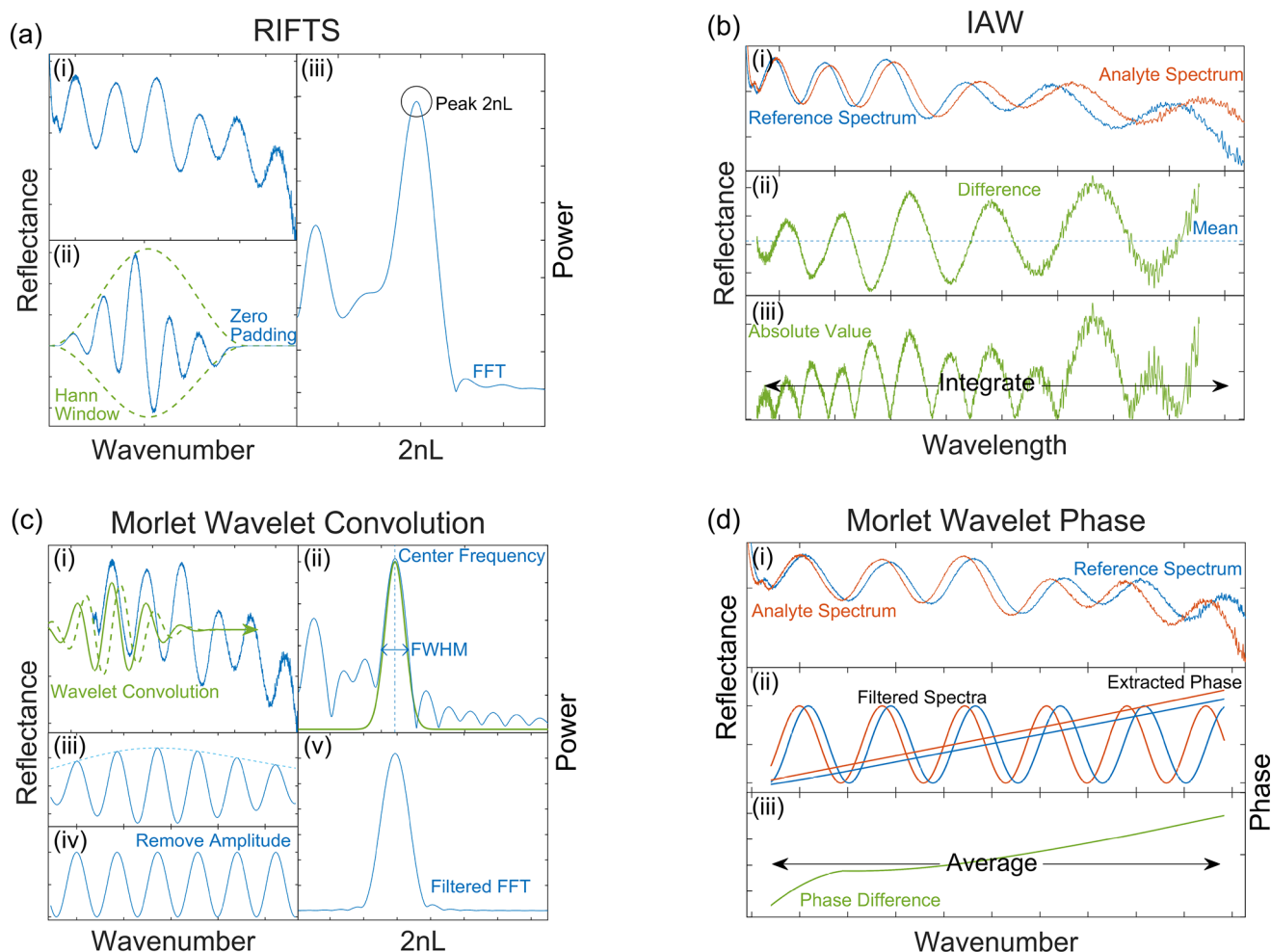


Figure 1. Illustration of signal processing techniques, (a) RIFTS, (b) IAW, (c) complex Morlet wavelet convolution, and (d) Morlet wavelet phase, applied to the experimentally measured reflectance spectra of a single-layer PSi thin film. The steps for each method are described in the text.

platforms. We utilize porous silicon (PSi) thin-film biosensors for our demonstration of the benefits of this signal processing approach. Because the characteristic pore size of PSi films is much smaller than the wavelength of light, PSi is treated as an effective medium, and the optical thickness and refractive index are referred to as the effective optical thickness and effective refractive index, respectively.¹⁵ PSi biosensors have an extraordinarily large capacity for biomolecule adsorption due to their vast surface area and strong interaction between light and adsorbed molecules. However, the lowest LODs achieved in the literature using PSi biosensors typically are higher than those based on other biosensing systems,^{16–18} in part due to the contributions of noise signatures that have not been mitigated, as well as mass transport challenges that have been recently investigated in other works.^{19–21}

The reflectance spectrum of a thin film contains a series of approximately sinusoidal Fabry–Pérot interference fringes. One common signal processing approach to measure changes in these fringes due to adsorbed biomolecules is the reflective interferometric Fourier transform spectroscopy (RIFTS) method,²² which involves determining the dominant frequency of these fringes by carrying out a fast Fourier transform (FFT) on the reflectance spectra and then identifying the peak interference fringe frequency. This method gives important physical information about the optical properties of the film, but its accuracy is deteriorated by noise. More recently,

promising improvements in LOD of PSi thin films have been reported^{23,24} using the interferogram average over wavelength (IAW) technique. However, the robustness of the IAW method is an issue when there are offset and amplitude variations modulating the Fabry–Pérot interference fringes. These noise sources, found in most data sets, originate from the measurement system (e.g., light source, spectrometer, and imperfect calibration of the system) as well as scattering of light by molecules adsorbed on the surfaces of the PSi thin film and on the surfaces of microfluidic channels when they are utilized.²⁵ Moreover, noise contributions tend to be more pronounced in sensing assays carried out in complex media.

Since the Fabry–Pérot fringes characteristic of thin-film reflectance spectra are approximately sinusoidal, they are well suited to band-pass filtering, designed to remove undesired low-frequency variations as well as white noise at all frequencies above and below the pass band, which improves robustness and enables lower detection limits. In this work, we show that the application of complex Morlet wavelet convolution, which has previously been used to filter electrical signals generated from electrodes monitoring brain or heart activity²⁶ and seismic activity,²⁷ is a highly effective approach to reduce noise signatures in the optical spectra of thin films such as PSi single-layer biosensors. We coin the name, “Morlet wavelet phase method”, to describe our approach that utilizes both a complex wavelet and extracted phase information. The

Morlet wavelet phase technique enables a reduction of the LOD by almost an order of magnitude relative to RIFTS and IAW and makes thin-film sensors, such as those based on PSi, potentially viable options for many clinical applications. We note that the Morlet wavelet phase signal processing technique does not negatively impact manufacturability, cost, complexity, or response time and can be applied alongside other sensitivity enhancing and noise reduction techniques.

SIGNAL PROCESSING APPROACHES

Several different signal processing approaches can be applied to help interpret measured optical spectra from thin films. For many applications, including biosensing, there is a particular interest in being able to determine small changes between two measured thin-film optical spectra. The reflectance spectrum of a thin film is characterized by Fabry–Pérot fringes²⁸ (e.g., Figure 1a(i)), which are caused by interference from successive reflections from the front and back faces of the film. The reflectance of a prototypical Fabry–Pérot etalon, R_{fp} is given in eq 1.

$$R_{fp} = \frac{2R(1 - \cos \phi)}{(1 - 2R\cos \phi + R^2)} \quad (1)$$

In this equation, R is the square of the reflection coefficient at a single interface (i.e., $R = |r|^2$, where r is the Fresnel amplitude reflection coefficient). The round-trip phase shift is given by $\phi = \frac{4\pi nL}{\lambda}$, where n is the refractive index of the thin film, L is the thickness of the film that must be less than the coherence length of the incident light, and λ is the wavelength of light. The derivation of eq 1 assumes negligible absorption and that the same material is adjacent to the front and back of the thin-film. The latter assumption is not strictly valid for many thin-film sensors, which often interface with a solution of biomolecules at the front surface and a substrate of different refractive index at the back surface. Accordingly, for many thin-film sensors, the intensity of reflected light will be modified from the ideal Fabry–Pérot etalon case and there may be a π phase shift in the Fabry–Pérot fringes. Nevertheless, the relationship indicated by eq 1 that minima in the reflectance spectra occur at $\phi = 2\pi m$, where $m = 0, 1, 2, \dots$, holds for all thin-film sensors. This phase relationship corresponds to wavelengths that satisfy the relation $2nL = m\lambda$. Hence, plotting R_{fp} against inverse wavelength (i.e., wavenumber) will yield a series of equally spaced sinusoidal fringes if no external noise sources are considered. The frequency of these fringes is $2nL$, which is known as the optical thickness. We note that since the independent variable, wavenumber, is in units of inverse distance, the frequency of the reflectance fringes is given, in this case, in units of distance. We additionally note that although the RIFTS, IAW, and Morlet wavelet phase methods are applied only to single-layer thin films in this work, these signal processing techniques could also be applied to analyze any signal containing a finite number of approximately sinusoidal frequency components.

RIFTS and IAW Methods. One approach to characterizing the reflectance spectra of thin films is to measure optical thickness by monitoring the frequency of the Fabry–Pérot fringes in wavenumber space. We note that it is essential to plot the reflectance of the film as a function of wavenumber so that the Fabry–Pérot fringes are equally spaced across the spectrum. Changes in optical thickness of thin films are characterized by changes in the frequency of these Fabry–

Pérot fringes. The RIFTS method aims to identify the dominant frequency of the Fabry–Pérot fringes, corresponding to the optical thickness, from the FFT of the reflectance spectra. The RIFTS technique consists of the following four operations:

1. Plot the reflectance spectra against the wavenumber using cubic spline interpolation to generate equally spaced points (Figure 1a(i)).
2. Apply a Hann window to the chosen spectral measurement range to enforce periodicity and consequently reduce spectral leakage (Figure 1a(ii)).
3. Increase the length of the data by zero padding to realize the desired resolution of $2nL$ values when the FFT is applied (Figure 1a(ii)). Note that the highest efficiency is achieved when the number of points is a power of 2.
4. Carry out an FFT and identify the frequency of the dominant peak (Figure 1a(iii)).

Changes in optical thickness caused by biomolecule attachment can therefore be determined in a straightforward manner, by monitoring the change in the peak frequency result from the RIFTS method applied to the spectra measured before and after exposure of the thin film to biomolecules.

Since a change in Fabry–Pérot fringe frequency causes the Fabry–Pérot fringes to shift (by an amount proportional to wavenumber), another strategy to measure biomolecule attachment is to calculate the difference between the spectra before and after biomolecule exposure. The IAW method uses this approach and is implemented as follows:

1. Find the difference between a “reference” reflectance spectrum before exposure of the target biomolecule and an “analyte” spectrum after biomolecule exposure, termed as the “interferogram” (Figure 1b(i)).
2. Zero the interferogram by subtracting the mean from each value (Figure 1b(ii)).
3. Integrate the absolute value of each point in the interferogram over the chosen spectral measurement range (Figure 1b(iii)).

It should be noted that the magnitude of the IAW signal change is strongly dependent on the changing amplitude of the Fabry–Pérot fringes at each given wavenumber in the reference and analyte spectra, which in turn makes the technique more susceptible to noise contributions that affect the measured amplitude of the spectra. The RIFTS technique, on the other hand, is not strongly affected by the relative amplitudes of the spectra.

Complex Morlet Wavelet Convolution: Morlet Wavelet Phase Method. Because the LOD for thin-film sensors is limited by both high-frequency white noise and low-frequency noise signatures in the reflectance spectrum, band-pass filtering is a promising signal processing approach to apply. In particular, complex Morlet wavelet convolution²⁹ is well suited for filtering the spectra of thin-film sensors as a means of maximally removing noise while retaining the desired optical signal. A complex Morlet wavelet is a complex exponential with a Gaussian envelope, which is localized in time and results in a Gaussian line shape in frequency space. The convolution of a Morlet wavelet with a signal is equivalent to multiplication in frequency space, which can act as a strict band-pass filter. Since the wavelet is complex, the filtered result is a complex signal from which phase and amplitude can be extracted. The first stage of the Morlet wavelet phase method, complex Morlet

wavelet band-pass filtering, is summarized by the following steps:

1. Plot the reflectance spectra against wavenumber using linear interpolation so points are equally spaced (Figure 1c(i)).
2. Zero pad the data to obtain the desired resolution in frequency space.
3. Carry out an FFT and identify the center frequency and full width at half-maximum (FWHM) of the dominant peak (Figure 1 (c) (ii)).
4. Use the center frequency and FWHM of the dominant peak to define a complex Morlet wavelet, shown in the green trace in Figure 1c(i) in wavenumber space. The FFT of the complex Morlet wavelet is shown in the green trace in Figure 1c(ii) and reveals the band-pass filtering ability of the Morlet wavelet. The spacing between wavenumber values of the wavelet should be the same as for the interpolated reflectance spectra.
5. Convolve the wavelet with the reflectance data (Figure 1c(i)) to obtain the complex-filtered output; the real part is shown in Figure 1c(iii).
6. The phase and amplitude can then be extracted from the real and imaginary components of the filtered output over the spectral measurement range; the extracted amplitude is shown in Figure 1c(iii) alongside the real part of the filtered output. The amplitude can subsequently be used to normalize the Fabry–Pérot fringes (Figure 1c(iii,iv)).

By carrying out an FFT of the uniform amplitude normalized fringes using a Hann window function, it becomes clear in frequency space that the high- and low-frequency noise components have been removed from the filtered data (Figure 1c(v)). For the Morlet wavelet phase method, only the phase is used, as this was found to be the most accurate way of transducing frequency shifts; however, for some applications, it may be useful to obtain normalized fringes, for example, as a preprocessing step to remove noise signatures before carrying out the IAW or RIFTS methods. The first three steps of complex Morlet wavelet band-pass filtering are calculated in a similar way to the RIFTS method, with the exception that no Hann window is applied to avoid broadening the dominant frequency peak (i.e., to give a more accurate FWHM of the frequency peak that is used in defining the wavelet) at the expense of having greater spectral leakage and extra lobes introduced. Additionally, through empirical studies, we found that linear interpolation gave the best performance for Morlet wavelet filtering, in contrast with the RIFTS method that performs best with cubic spline interpolation.

The Morlet wavelet phase method³⁰ uses complex Morlet wavelet filtering to measure changes in optical thickness as follows:

1. Apply complex Morlet wavelet band-pass filtering, as described previously, to a “reference” reflectance spectrum before exposure of the target biomolecules and to an “analyte” spectrum after biomolecule exposure (Figure 1d(i)). The real part of the filtered output is shown in Figure 1d(ii).
2. After extracting the phase from the complex results of filtering the reference and analyte spectra (step 6 in Morlet wavelet band-pass filtering), unwrap the phase by adding 2π every time it goes through another complete cycle to give a continuous linearly increasing phase,

rather than being confined to the interval $[0,2\pi]$, for both the reference and analyte spectra (Figure 1d(ii)).

3. Correct for the phase of the reference and analyte spectra starting in different cycles. For example, if the initial phase of the reference spectra at the lowest wavenumber in the measurement window has a phase just below 2π , biomolecule adsorption could cause the initial phase to shift into the next cycle with a phase just above 0 for the analyte spectra, which causes an additional 2π difference between the reference and analyte phase at every value of wavenumber, unrelated to biomolecule adsorption. To correct for this difference in the initial phase of the reference and analyte spectra, a coarse value of the initial phase is estimated using the FFT dominant fringe frequency, alongside the accurate Morlet wavelet extracted phase, to determine when the phase has entered a different cycle. The coarse estimate can be defined as $2nL/\lambda_{\text{end}}$, where $2nL$ is the optical thickness given by the RIFTS method and λ_{end} is the higher wavelength bound for the spectral measurement range. The fine estimate is the extracted phase from the Morlet wavelet-filtered signal at the lowest value of wavenumber, $1/\lambda_{\text{end}}$. The difference between coarse and fine estimates for the reference and analyte spectra is compared; when they differ by a multiple of 2π , this is corrected.
4. Average the difference between the unwrapped linear phase for the reference and target spectra, which yields the Morlet wavelet phase result (Figure 1d(iii)).

To optimize the performance of all three signal processing methods (RIFTS, IAW, and Morlet wavelet phase), the spectral measurement range to analyze should be chosen to include as much of the measured spectra as possible while rejecting the extremes of the spectra with a poor signal-to-noise ratio (S/N). Hence, the most appropriate spectral range for the signal processing methods is dependent on the limitations of the optical components and spectrometer utilized in the measurements. In this work, a spectral measurement range of 500–800 nm was used unless otherwise noted in order to facilitate a comparison between techniques and previous studies.

Computational Generation of Spectra. To provide a comprehensive comparison between different signal processing techniques, the reflectance spectra of a single-layer P*Si* thin film were simulated using the transfer matrix method.²⁸ White Gaussian noise was added to the simulated spectra to better mimic measured data. The simulated thin film was defined as a 2.4 μm -thick layer with an effective refractive index of 1.2, which are realistic parameters comparable with experimental data sets. To rigorously test each signal processing method and mirror noise encountered in real experimental spectra as closely as possible while keeping the analysis simple and generalizable, three different noise contributions were considered: (1) a simple shift of the Fabry–Pérot fringes due to a refractive index change with added white Gaussian noise, (2) a refractive index change with white Gaussian noise and a unitary wavelength-dependent linear offset applied to the Fabry–Pérot fringes, and (3) a refractive index change with white Gaussian noise and a unitary wavelength-dependent linear amplitude variation applied to the Fabry–Pérot fringes. These noise contributions can be expressed as

$$f(\lambda) = R(\lambda) \left(1 + a \frac{(\lambda - \lambda_{\text{start}})}{(\lambda_{\text{end}} - \lambda_{\text{start}})} \right) + o \frac{(\lambda - \lambda_{\text{start}})}{(\lambda_{\text{end}} - \lambda_{\text{start}})} + \sigma_n \quad (2)$$

where $R(\lambda)$ is the wavelength-dependent reflectance generated using the transfer matrix method, a is the amplitude variation term, o is the offset variation term, σ_n is the white Gaussian noise term, λ_{end} and λ_{start} are the upper and lower bounds of the wavelength measurement range, respectively, and $f(\lambda)$ is the resulting noisy spectra. The S/N when comparing the signal to the white Gaussian noise was 27.7 dB. The S/Ns decreased to 7.9 and 7.7 dB when the linear offset was superimposed or the linear amplitude variation was introduced, respectively. A linearly varying offset and amplitude are simple modifications to fringes with a relatively complex spectral composition, testing the signal processing methods' immunity to a wide variety of noise signatures seen experimentally.

MATLAB (R2019b) was used to generate the noisy spectra. In addition, the signal processing toolbox in MATLAB was utilized to implement each of the signal processing algorithms investigated in this work. We note that the algorithmic code run on simulated data and experimental data from both labs was identical.

Limit of Detection. The LOD of a biosensor is the minimum concentration or number of molecules that can be reliably detected. A normal distribution of measurements can be built up both before and after biomolecule exposure, termed as the blank and shifted distributions, respectively. The LOD is typically quantified as the concentration of the target molecule leading to a response such that the lower bound of the highest 5% of the blank distribution, which lies at 1.65 standard deviations above the mean, coincides with the upper bound of the lowest 5% of the shifted distribution, which lies at 1.65 below the mean.³¹ Equivalently stated

$$\mu_{\text{shift}} - \mu_{\text{blank}} = 1.65\sigma_{\text{blank}} + 1.65\sigma_{\text{shift}} \approx 3.3\sigma_{\text{blank}} \quad (3)$$

where μ_{blank} and μ_{shift} are the mean of the blank and shifted distributions, respectively, and σ_{blank} and σ_{shift} are the standard deviations of the blank and shifted distributions, respectively. The standard deviations are typically assumed to be approximately equal. When introducing the offset or amplitude gradient, the resulting change in the response was isolated by calculating the blank distribution with and without the gradient at a constant refractive index. The effect on the response of each signal processing technique when applying a gradient to the offset or amplitude, Δg , was added to the blank-distribution standard deviation, σ_{blank} , resulting in an LOD of $3.3(\sigma_{\text{total}})$, where $\sigma_{\text{total}} = \sigma_{\text{blank}} + \Delta g$.

Including this effect as part of the standard deviation of the blank distribution enables modeling a distribution of offset or amplitude gradients, that occur in tandem with any refractive index change and white noise-induced interference fringe shifts. The mean and standard deviation of the blank and shifted distributions, as well as the blank distributions incorporating an offset or amplitude gradient, were each calculated from 1000 separately generated spectra with a random white noise contribution.

■ EXPERIMENTAL METHODS

Signal processing approaches were applied to the measured data from two experimental systems: (1) nonspecific bovine serum albumin (BSA) assay in buffer to investigate the LOD and (2) an anterior

gradient 2 (AGR2) protein biosensor to investigate (i) the robustness of the signal processing approaches in buffered and complex media and (ii) selectivity in comparing target and nontarget proteins. Nonspecific adsorption of BSA is commonly utilized to demonstrate the proof-of-concept performance of biosensing platforms, and AGR2 is a biomarker for many types of cancer. These assays were executed in different labs (Vanderbilt University and Technion Israel Institute of Technology), with different experimental setups, different experimental procedures, and different materials, to demonstrate the broad applicability of the Morlet wavelet phase technique when encountering different noise fingerprints.

BSA Assay (Carried Out at Vanderbilt). *Materials.* Chemicals were all analytical grade and used without further purification. Deionized (DI) water with a resistivity of 15 M Ω cm from a Millipore Elix water purification system was used for all solutions. Single side polished, boron-doped silicon wafers (<100>, 0.01–0.02 Ω cm, 500–550 μ m) were purchased from Pure Wafer. Ethanol and BSA were purchased from Thermo Fisher Scientific, and a pH 4 reference standard buffer, used for BSA solutions, was obtained from Sigma-Aldrich. Aqueous hydrofluoric acid (HF) (48–51%) was purchased from Acros Organics. Solution pH was measured using a Mettler Toledo Seven Easy pH meter.

Fabrication of Single-Layer PSi. Single-layer PSi thin films were fabricated by anodic etching of p-type silicon wafers with HF, described in detail elsewhere.^{15,32} A solution of 15% (v/v) HF in ethanol was used, and the wafer was etched using an Advanced Micromachining Tools (AMMT) MPSB porous silicon wafer etching system. First, a sacrificial layer was etched with a current density of 70 mA cm⁻² for 100 s and then dissolved in 1 M KOH solution. Next, the sample was thoroughly cleaned with DI water and ethanol and then etched again at 70 mA cm⁻² for 50 s. Finally, the wafer was oxidized in ambient air at 800 °C for 10 min using a Lindberg/Blue M box furnace to passivate the silicon by forming an insulating layer of SiO₂. The PSi films were 1.77 μ m-thick, with a porosity and average pore diameter of 67% and 49 nm, respectively, as determined by scanning electron microscopy (SEM) image analysis and effective optical thickness measurements.

Optical Reflectance Measurements. Light from a quartz tungsten halogen light source from Newport was coupled into an optical fiber, which is split before entering a lens tube housing and Olympus SPlan 10x microscope objective lens. The height of the lens relative to the PSi sample was adjusted to focus the light to a spot size of approximately 5 mm diameter on the surface of the PSi films. The reflected light was then collected by the same lens and coupled by another optical fiber into an Ocean Optics USB4000 CCD spectrometer, outputting the spectra to a PC running the Ocean Optics Spectra Suite software.¹⁵ A total of 100 spectra were averaged and recorded once per second for each measurement.

Experimental Procedure. PSi samples (5 mm \times 5 mm) were cleaved from the etched wafer, washed with water and ethanol, and dried under a stream of nitrogen. Reflectance spectra were then measured to obtain a baseline effective optical thickness and IAW and Morlet wavelet phase reference spectra. Further 100 measurements were taken to quantify the noise floor for each method: the blank distribution standard deviation, σ_{blank} . Different concentrations of BSA were prepared in 80% pH 4 reference standard buffer, 20% DI water solutions v/v (3 pM, 300 pM, 30 nM, 300 nM, 3 μ M, 30 μ M, and 300 μ M) and were drop cast on the samples and left to incubate for 2 h. The samples were subsequently washed in a water bath for 10 s, which removes unbound and potentially a small number of weakly bound molecules in the pores and from the surface. The reflectance change after this wash step showed almost no dependence on wash duration. After washing, the PSi was dried under a stream of nitrogen and measured again. There were 16 repeats performed at each concentration. A number of adsorption isotherms were fit to the data using a least-squares fit weighted by the variance due to the heteroscedasticity of the data, and the chi-squared goodness of fit was calculated to quantify the quality of the model fit and determine the most appropriate adsorption model. The predicted LOD was then calculated, given by the concentration where the best fit line intersects

Table 1. LOD in Refractive Index Units (RIU) for Several Signal Processing Techniques Applied to Single-Layer PSi Reflectance Data Generated Computationally Using the Transfer Matrix Method with Added Noise

	Simple refractive index change	Refractive index change with linearly varying offset	Refractive index change with linearly varying amplitude
RIFTS	8.2×10^{-4}	2.5×10^{-3}	8.9×10^{-4}
IAW	3.9×10^{-4}	1.7×10^{-3}	1.9×10^{-2}
Morlet wavelet phase	5.7×10^{-5}	1.3×10^{-4}	7.4×10^{-5}

$3.3\sigma_{\text{blank}} + I$, where I is the intercept of the adsorption model line of best fit.

AGR2 Biosensor (Carried Out at Technion). *Materials.* Chemicals were all analytical grade and used without further purification. Double distilled water (ddH₂O) with a resistivity of 18.2 MΩ·cm from a Milli-Q water purification system was used for all solutions. Heavily p-doped silicon wafers (<100>, 0.90–0.95 mΩ cm) were purchased from Siltronix Silicon Technologies. Aqueous 48% HF and ethanol were purchased from Bio-Lab Ltd. (3-Aminopropyl)triethoxysilane (APTES), diisopropylethylamine (DIEA), succinic anhydride, *N*-(3-dimethylaminopropyl)-*N'*-ethylcarbodiimide hydrochloride (EDC), *N*-hydroxysuccinimide (NHS), acetonitrile, and all buffer salts were supplied by Merck. The anti-AGR2 aptamer sequence,³³ 5'-TCT-CGG-ACG-CGT-GTG-GTC-GGG-TGG-GAG-TTG-TGG-GGG-GGG-GTG-GGA-GGG-TT-3', was purchased with a 5'-amino modification from Integrated DNA Technologies. The AGR2 protein was purchased from MyBioSource Inc. Rabbit immunoglobulin G (IgG) was purchased from Jackson ImmunoResearch Labs Inc. Human blood plasma from healthy subjects was purchased from Merck. Selection buffer (SB) was composed of 137 mM NaCl, 20 mM KCl, 10 mM Na₂HPO₄, and 2 mM KH₂PO₄ (pH 7.4).

Fabrication of Single Layer PSi. Single-layer PSi thin films were fabricated by anodic etching of p-type silicon wafers with HF. First, a sacrificial layer was etched with a current density of 300 mA cm⁻² for 30 s, using 3:1 (v/v) aqueous HF to ethanol solution, and then dissolved in 0.1 M NaOH solution to remove surface impurities and oxides. Another layer is formed using identical conditions to the sacrificial layer, and the resulting PSi films were thermally oxidized at 800 °C for 1 h in a Thermo Scientific, Lindberg/Blue M Split-Hinge tube furnace. The PSi film thickness and range of pore sizes were measured with a Carl Zeiss Ultra Plus high-resolution SEM system at an accelerating voltage of 1 keV and were found to be ~4.9 μm and 40–60 nm, respectively, and the average porosity was determined to be 74% using the spectroscopic liquid infiltration method (SLIM).³⁴

Surface Chemistry Preparation. Amino-terminated aptamers, consisting of the anti-AGR2 sequence, were attached to the surface of the PSi films by carbodiimide coupling chemistry and amino silanization, as detailed elsewhere.^{35,36} Briefly, the oxidized PSi films were amino-silanized in a solution of 1% APTES and 1% DIEA in ddH₂O (v/v) for 1 h and annealed at 100 °C for 15 min. Subsequently, surface carboxylation was carried out in a solution of 10 mg mL⁻¹ succinic anhydride and 2% (v/v) DIEA in acetonitrile for 3 h followed by surface activation with 10 mg mL⁻¹ EDC and 5 mg mL⁻¹ NHS in 0.5 M MES buffer (pH 6.1) for 1 h. The activated surface was then reacted with the 50 μM amino-terminated aptamers for 1 h followed by blocking with Tris buffer (50 mM Tris base, pH 7.4).

Optical Reflectance Measurements. For the biosensing experiments, the anti-AGR2 aptasensor was mounted in a custom-made

Plexiglas cell, detailed elsewhere.³⁷ Light from a tungsten light source was coupled using a bifurcated optical fiber into an objective lens and focused onto the center of the PSi sample with a spot size of approximately 1 mm². The reflected light was collected through the same fiber into an Ocean Optics USB4000 CCD spectrometer.

Experimental Procedure. All experiments were performed without flow, in a static mode. First, a baseline was established by incubating the aptasensor in SB. Next, an AGR2 protein solution either in SB or in 50% blood plasma in SB was injected into the cell and incubated on top of the sample for 1 h. It should be noted that the blood plasma was diluted 1:1 in SB to ensure the aptamer's proper folding and functionality in the complex media. Finally, the sample was washed with SB with a volume of ~10 mL until equilibrium was reached and all unbound molecules were removed.

RESULTS AND DISCUSSION

Simulation Results Comparing the LOD of Different Signal Processing Techniques. The minimum detectable refractive index change of a thin film was calculated by applying different signal processing techniques to the reflectance spectra simulated using the transfer matrix method with additive white Gaussian noise. In order to systematically evaluate the robustness of the signal processing techniques to noise contributions often arising during experimental measurements, the LOD analysis was carried out with (1) no added systematic noise contributions, (2) a linearly varying signal offset, and (3) a linearly varying amplitude increase. As shown in Table 1, the Morlet wavelet phase technique achieves a substantially lower LOD than both RIFTS and IAW methods in all cases.

We note that all the signal processing techniques perform proportionally better when the white noise is reduced. In order to determine this effect of S/N on the performance of the different signal processing techniques, the LOD was calculated as a function of white Gaussian noise, which was varied by two orders of magnitude. A linear relationship was found between the S/N and LOD for each signal processing technique, such that the relative merit of the techniques shown in Table 1 can be considered independent of the Gaussian noise level. The RIFTS method performs relatively poorly in the presence of offset variations since the maximum of the dominant fringe frequency peak is shifted by the superposition of lower frequency components. On the other hand, the LOD for RIFTS is almost unchanged for amplitude variations, which only change the power of the dominant fringe frequency peak rather than its position. The IAW method is negatively affected

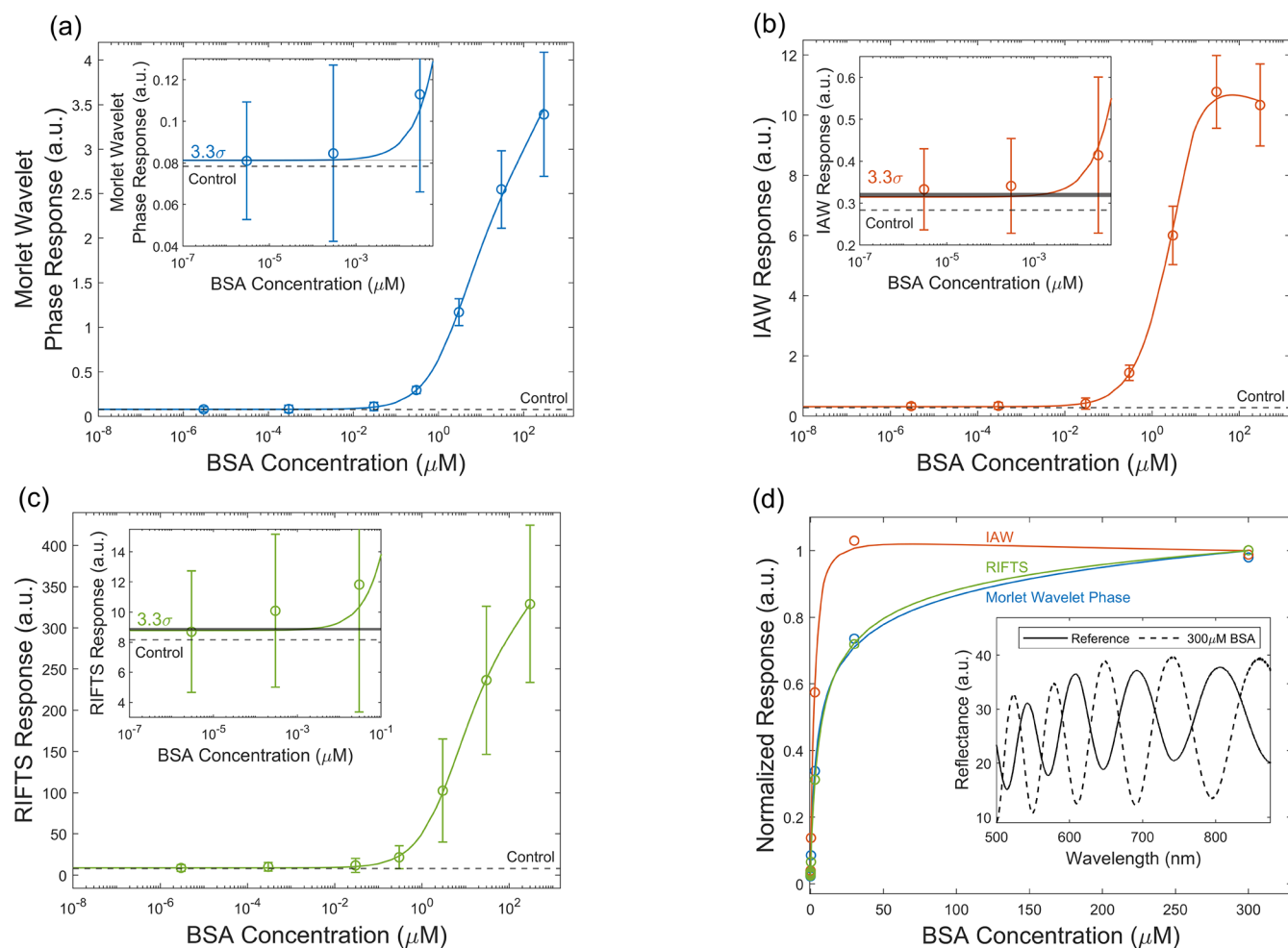


Figure 2. Results of exposing a single layer of oxidized PSi to solutions of BSA in buffer, with concentrations between 0 and 300 μM , analyzed using (a) Morlet wavelet phase, (b) IAW, and (c) RIFTS signal processing methods, shown on a semi-log plot. A Redlich–Peterson adsorption isotherm line of best fit is overlaid, as well as the noise floor for each method. The insets show the data, noise floor, and the trend line in the region of the LOD. (d) Normalized responses of all signal processing techniques as a function of BSA concentration on a linear scale; inset is an illustration of the maximum shift caused by 300 μM BSA exposure.

by both offset and amplitude variations; both increase the difference between fringes, which manifests as spurious contributions to the IAW signal. In contrast, the Morlet wavelet phase method gives a comparably low LOD with and without offset or amplitude variations. This reduced sensitivity to noise is a result of the Morlet wavelet convolution, which is an effective technique for filtering thin-film interference fringes because it acts as a very strict band-pass filter. The shape of a Morlet wavelet closely resembles the shape of Fabry–Pérot fringes in terms of fundamental frequency constituents.

Additionally, due to dispersion, the Fabry–Pérot fringe frequency will not be constant across the spectra; the Morlet wavelet filtering is able to capture this variation because it is localized in wavenumber, while the RIFTS and IAW methods process the data across the spectra simultaneously. Other than noise immunity, complex Morlet wavelet convolution also provides an integrated way of extracting and therefore normalizing amplitude variations; other filtering methods require an additional step, such as applying the Hilbert transform. Furthermore, the inclusion of an FFT in the signal processing pipeline has another advantage, which is a coarse frequency indicator enabling an unlimited measurement range. The IAW method, which does not utilize an FFT, is thus

limited to measuring relatively small spectral shifts, particularly when the reference fringe frequency is high: the IAW signal starts to decrease once the peaks of the analyte spectra shift further than the valleys of the reference spectra.

While Table 1 compares only RIFTS, IAW, and Morlet wavelet phase, additional signal processing approaches were considered. Other techniques such as summing of the cross-correlation between a reference and shifted spectra, least-squares fitting of the Fabry–Pérot fringe functional form (eq 1), super-resolution frequency estimation techniques such as the multiple signal classification (MUSIC) algorithm, and finite impulse response (FIR) band-pass filtering in conjunction with the Hilbert transform were investigated but did not perform as well as the Morlet wavelet phase method. While the computational complexity of the Morlet wavelet phase method may initially appear to be a potential concern for future point-of-care applications, given the combined steps of an FFT, wavelet convolution, and phase difference calculation, embedded implementation of real-time FFT and wavelet convolution algorithms have been realized.³⁸ Accordingly, no insurmountable difficulty is anticipated in designing an instrument using these techniques that can update its readout

every few seconds, particularly since such computation time is negligible compared to sensor response times.

Further reduction in an achievable LOD with the Morlet wavelet phase technique could be achieved by using a thicker film, optimizing wavelet parameters, and tuning the range of filtered data. Thicker films have higher frequency Fabry–Pérot fringes and an increased optical thickness, which enables better discrimination between the desired signal frequency and unwanted low-frequency noise contributions.

However, thick PSi layers may suffer from mass transport challenges that result in longer response times and sensitivity limitations. Mitigation of these challenges may be possible by using larger pore diameters, mixing approaches, and flow through configurations;^{19,20} however, selecting the most appropriate PSi thickness ultimately depends on a balance between noise mitigation and mass transport limitations. A lower LOD may also be achievable by optimizing the width of the wavelet. In this work, the width of the wavelet was intuitively selected to be equivalent to the FWHM of the dominant FFT peak to enable maximum generalizability to any given system. However, there is no fundamental reason why choosing this width would provide the best rejection of noise while retaining the maximum useful portion of the signal. The optimum width of the wavelet depends on the nature of the noise of the system: if the noise is closer in frequency content to the fringe frequency, a narrower wavelet width will provide a better signal-to-noise ratio, and vice versa. In this investigation, the range of spectral data filtered and processed is the same for all signal processing techniques. However, in practice, some sensing systems will benefit from filtering a wider range of spectral data but then discarding sections of filtered data at the highest and lowest wavenumber values before processing and obtaining the Morlet wavelet phase result. Finally, higher resolution of the interpolated data and wavelet will improve accuracy at the expense of computational complexity, which is a trade-off governed by sensor performance requirements.

Comparison of Different Signal Processing Techniques Applied to Experimental Data. BSA Assay. The LOD achievable through application of each of the signal processing methods to an experimentally obtained data set was investigated by exposing PSi thin-film sensors to a series of BSA concentrations, from 0 to 300 μM . The spectra were analyzed, and several adsorption isotherms³⁹ were fitted to the data using nonlinear regression. We assumed that the measurements were independent and normally distributed while recognizing the heteroscedasticity of the data. As a result, the adsorption model fit required the minimization of the sum of the squared residuals weighted by the inverse of the variance, according to maximum likelihood estimation.

The Redlich–Peterson adsorption isotherm, which is applied to calculate the trend lines shown in (Figure 2), was the best fit to the data, as determined by calculating the reduced chi-squared goodness of fit metric. This adsorption isotherm model implies imperfect monolayer adsorption. The Redlich–Peterson isotherm is of the form shown in eq 4:

$$\theta = I + \frac{AC_e}{1 + BC_e^\beta} \quad (4)$$

where θ is the response of the signal due to biomolecule adsorption, C_e is the equilibrium concentration of BSA solution, and the fitting parameters are the following: I , the intercept or predicted response to a pure buffer control, A , the

Redlich–Peterson isotherm constant, B , a constant, and β , a constant between 0 and 1. The IAW line of best fit is complicated by the inherent nonlinearity of the method, as evidenced by the IAW response decreasing when the BSA concentration is increased from 3 to 300 μM (Figure 2b). The Morlet wavelet phase and RIFTS responses, which are linear, show that this concentration range is nearing the saturation region (Figure 2a,c), and thus the response should continue to increase in this range. The apparently different trend for IAW can be accounted for by observing that the largest spectral shift for a concentration of 300 μM exceeds the free spectral range limit of the IAW method (Figure 2d, inset). To take the nonlinearity into account, the deviation from a linear response as a function of percentage change in RIFTS response was determined by simulation using the transfer matrix method and was fitted with a second-order polynomial. The adsorption isotherm was then scaled by this nonlinearity using the measured percentage change in RIFTS response but was otherwise fitted to the data in the same way as the other methods. The LOD was determined by finding the concentration at which the Redlich–Peterson adsorption isotherm line of best fit exceeds its intercept by $3.3\sigma_{\text{blank}}$, the noise floor in the blank. The fitting parameters and LOD for the RIFTS, IAW, and Morlet wavelet phase methods are shown in Table 2, and the data, the Redlich–Peterson

Table 2. LOD for BSA Exposure Analyzed Using IAW, RIFTS, and Morlet Wavelet Phase Signal Processing Methods, Showing Noise Level and Redlich–Peterson Adsorption Isotherm Fit Parameters

approach	3.3σ (a.u.)	LOD (nM)	I (a.u.)	A (LM^{-1})	B (LM^{-1})	β
RIFTS	1.62×10^{-1}	3.2	8.78	50.16	0.24	0.92
IAW	1.00×10^{-2}	2.5	0.32	4.02	0.37	0.95
Morlet wavelet phase	1.85×10^{-4}	0.2	0.08	0.82	0.47	0.88

adsorption isotherm line of best fit, and the noise floor for each method are shown in Figure 2. The Redlich–Peterson adsorption model simplifies to the Langmuir isotherm when $\beta = 1$. For all three signal processing methods, the optimal value for β is close to 1, suggesting only a small perturbation from ideal monolayer formation on a homogenous surface.

The relative differences in LOD values between the signal processing techniques seen experimentally (Table 2) are in good agreement with the theoretical predictions of Table 1. Since the BSA assay is a simple experiment in buffer solution, the presence of noise signatures is minimal and compares favorably with the simple refractive index change case in Table 1. The lowest LOD achievable for BSA is 200 pM (4 femtomoles in a 20 μL solution) when the Morlet wavelet phase method is applied, which is one order of magnitude lower than those for IAW and RIFTS methods. The LOD values shown in Table 2 are not as low as those recently reported in the literature for a PSi sensor.²⁴ The predominant reason lies in the method of calculating the LOD. A common practice is to center the noise floor around 0, rather than centering the noise floor around the intercept of the line of best fit. However, centering the noise floor around 0 is misleading because if the intercept is increased, the LOD can be artificially decreased and, moreover, the LOD becomes undefined when the intercept is outside the noise floor. Hence,

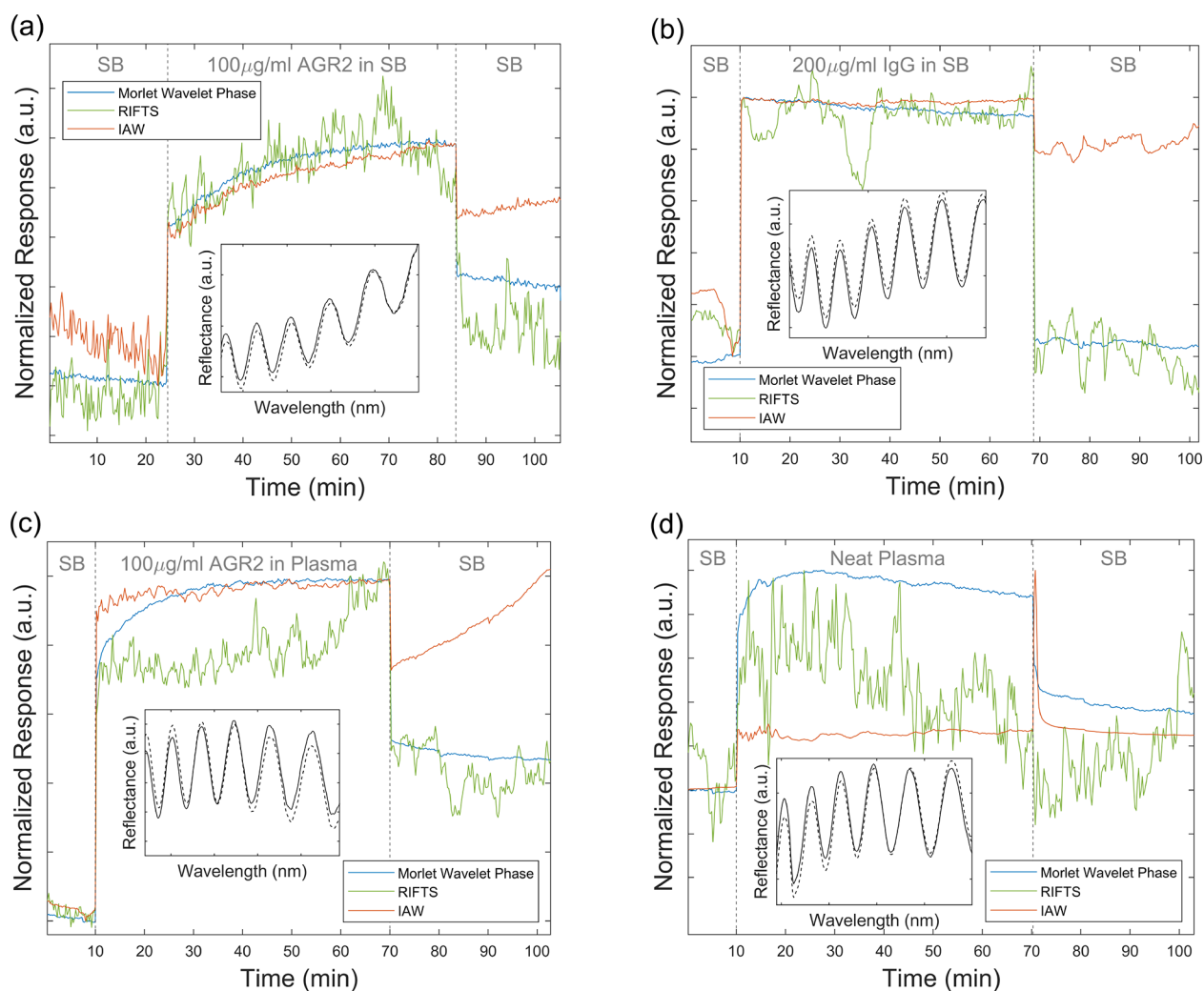


Figure 3. Comparison of signal processing techniques applied to experimental data collected by exposing the single-layer PSi biosensor to (a) $100 \mu\text{g mL}^{-1}$ AGR2, the target protein, in buffer solution, (b) $200 \mu\text{g mL}^{-1}$ nontarget protein IgG in buffer, (c) $100 \mu\text{g mL}^{-1}$ AGR2 spiked in 50% plasma in buffer, and (d) 50% neat plasma in buffer. In all cases, there are pre- and post-wash steps in buffer. Insets show the reflectance spectra taken during the pre- and post-wash steps; signal offset and amplitude variations (i.e., noise signatures) can be observed.

the method we use for calculating the LOD in this paper is a more conservative, and importantly, a more robust approach, and is consistent with the formulation defined by IUPAC and others.^{31,40} A similar LOD to that reported here is obtained when this approach (i.e., centering the noise floor at the intercept) is applied to other comparable published data sets.²⁴

AGR2 Assay. The robustness of the Morlet wavelet phase method to low-frequency offset and amplitude variations, in comparison to the RIFTS and IAW methods, was investigated through the application of the signal processing techniques to experimental data of an aptamer-based single-layer PSi biosensor. This biosensor is designed to selectively target the AGR2 protein and consists of oxidized PSi thin films, in which amino-terminated anti-AGR2 aptamers³³ are immobilized via NHS/EDC coupling chemistry.³⁶ Reflectance measurements of the biosensor upon exposure to the target AGR2 protein and nontarget IgG protein (at a concentration of 100 and 200 $\mu\text{g mL}^{-1}$, respectively) in buffer solution and 100 $\mu\text{g mL}^{-1}$ AGR2 in plasma were carried out. The reflectance data shown in the insets of Figure 3 reveal that both offset and amplitude variations are present in the measured data. We note that the magnitude of the RIFTS, IAW, and Morlet wavelet phase

processed signals were normalized to lie within the same range for ease of comparison. Common trends are shown in the data processed with RIFTS, IAW, and Morlet wavelet phase: (1) a relatively stable baseline value is established during buffer solution incubation, (2) a large increase in signal magnitude occurs when the AGR2, IgG protein, or plasma alone is introduced due to the change in the refractive index of the introduced solution compared to the baseline buffer and diffusion into the pores, (3) as the solution is incubated on top of the PSi, for solutions containing AGR2, there is a more gradual increase in the signal due to the target protein binding to the aptamers immobilized on the pore walls, conversely for control solutions, a negligible additional signal change occurs, (4) a signal reduction occurs when a buffer rinse is carried out to remove unbound protein from the pores, and (5) a relatively stable new baseline value is established in most cases upon incubating the sample with buffer solution once again. Key differences in the S/N, ability to resolve protein capture dynamics, and accuracy of the biosensing result can be seen by comparing the signals processed by RIFTS, IAW, and Morlet wavelet phase methods in Figure 3. When using RIFTS, the noisy signal makes it difficult to determine the magnitude of

the signal change due to protein capture with high accuracy and also makes it more challenging to ascertain target protein capture dynamics. Low-frequency noise signatures lead to false trends for protein capture in IAW data, which is of significant concern for the accuracy of the P*Si* biosensor. In Figure 3b, the IAW method suggests that there is a large signal change when the sensor is exposed to the nontarget protein, giving a false positive result. In Figure 3d, artifacts in the IAW signal are present due to the IAW response predominantly to offset changes. Moreover, in Figure 3a,c, the IAW method suggests an unexpected continually increasing signal during the post-protein exposure buffer rinse, and incubation, which is not consistent with the RIFTS and Morlet wavelet phase results and is physically misleading. Such an increase in the optical signal would typically be attributed to molecules diffusing into the porous layer leading to a corresponding increase in the P*Si* effective refractive index; however, no protein is present in the solution on top of the biosensor at this stage.²⁰ It is important to note that because the IAW-processed response can be dominated by the change in the offset and amplitude of the reflectance spectra, instead of by frequency shifts that are present due to molecular attachment, caution must be taken to eliminate systematic noise sources in experiments when utilizing the IAW method. Otherwise, it is possible that the IAW result may be disconnected from the physics of the system, as exemplified in Figure 3c,d. We note that the data presented in Figure 3 are representative of all the data collected: the IAW response exhibited artifacts or a false response that did not reflect the physical system in more than 50% of all experiments and in 100% of the nonspecific protein experiments.

In all cases studied in Figure 3, the Morlet wavelet phase method is shown to be the most robust and reliable signal processing approach. There is a clear distinction between signal changes for target protein capture, a negligible signal change when the biosensor is exposed to a nontarget protein in buffer and a small nonspecific binding-induced signal change when the biosensor is exposed to nonspecific plasma. While the Morlet wavelet phase and RIFTS signal processing techniques led to similar final results for most biosensing experiments, the Morlet wavelet phase signal has a much higher S/N ratio than the RIFTS signal, which should lead to a lower experimentally demonstrated LOD. Moreover, the Morlet wavelet phase method clearly elucidates the target protein capture dynamics.

CONCLUSIONS

Applying the Morlet wavelet phase technique, which is based on complex Morlet wavelet band-pass filtering and calculation of the average phase difference, to P*Si* thin-film biosensor reflectance data provides a robust, low-noise measure of frequency shifts that arise due to biomolecular recognition and binding events in the pores. The key benefits of the Morlet wavelet phase method are reducing the effect of noise present across the frequency spectrum and mitigating spurious signal changes that otherwise result from low-frequency variations in the offset and amplitude of measured spectra. Analysis of both simulated data and experimental data from a BSA assay demonstrate that the Morlet wavelet phase method achieves an LOD that is approximately one order of magnitude lower than that of RIFTS and IAW, two other signal processing approaches used to analyze data from P*Si* thin-film sensors and biosensors. Moreover, it was shown that the Morlet wavelet phase method can be reliably applied to noisy data

acquired in complex biological media. Improved S/N and selectivity were demonstrated by applying the Morlet wavelet phase method to data from an aptamer-based biosensor for targeting a cancer biomarker, AGR2 protein, compared to the application of RIFTS and IAW to the same data set. The robustness and lower detection limit achievable by employing the Morlet wavelet phase signal processing technique can benefit many applications where noise in data sets cannot be perfectly controlled and low detection limits are required for clinical relevancy.

AUTHOR INFORMATION

Corresponding Author

Sharon M. Weiss – Department of Electrical Engineering and Computer Science, Vanderbilt University, Nashville, Tennessee 37235, United States; orcid.org/0000-0003-2252-3104; Email: sharon.weiss@vanderbilt.edu

Authors

Simon J. Ward – Department of Electrical Engineering and Computer Science, Vanderbilt University, Nashville, Tennessee 37235, United States; orcid.org/0000-0003-0915-7584

Rabeb Layouni – Department of Chemical and Biomolecular Engineering, Vanderbilt University, Nashville, Tennessee 37235, United States; orcid.org/0000-0002-2416-7417

Sofia Arshavsky-Graham – Department of Biotechnology and Food Engineering, Technion Israel Institute of Technology, 32000 Haifa, Israel

Ester Segal – Department of Biotechnology and Food Engineering, Technion Israel Institute of Technology, 32000 Haifa, Israel; orcid.org/0000-0001-9472-754X

Complete contact information is available at: <https://pubs.acs.org/10.1021/acssensors.1c00787>

Author Contributions

All authors have given approval to the final version of the manuscript.

Funding

NIH grant # R21AI156693 and the Israel Science Foundation (grant no. 704/17).

Notes

The authors declare no competing financial interest.

ACKNOWLEDGMENTS

A freely downloadable, user-friendly application is posted on GitHub (<https://weissgroupvanderbilt.github.io/MorletWaveletPhaseApp/>), which will perform the Morlet wavelet phase analysis on data sets input by users without requiring any licensed software, alongside a test data set, similar to those analyzed in this manuscript, and a readme file with user instructions. Links are also provided on the Weiss group website (<https://my.vanderbilt.edu/vuphotonics/resources>), also including the test data set and readme file. Additionally, a freely downloadable MATLAB toolbox entitled “Morlet Wavelet Phase” is available on the MATLAB file exchange, allowing users to run the code in MATLAB. The authors thank Xiang Zhou for his work developing the application. The authors also thank Dr. Catie Chang and Dr. D. Mitchell Wilkes for helpful discussions related to signal processing.

■ ABBREVIATIONS

LOD, limit of detection; PSi, porous silicon; RIFTS, reflective interferometric Fourier transform spectroscopy; FFT, fast Fourier transform; IAW, interferogram average over wavelength; FWHM, full width at half-maximum; S/N, signal-to-noise ratio; AGR2, anterior gradient 2; HF, hydrofluoric acid; IgG, immunoglobulin G; SB, selection buffer; SEM, scanning electron microscopy; DI, deionized; BSA, bovine serum albumin; MUSIC, multiple signal classification; FIR, finite impulse response

■ REFERENCES

- (1) Lee, S.; Huang, H.; Zelen, M. Early Detection of Disease and Scheduling of Screening Examinations. *Stat. Methods Med. Res.* **2004**, *13*, 443–456.
- (2) Lanphear, B. P. Low-Level Toxicity of Chemicals: No Acceptable Level. *PLoS Biol.* **2017**, *15*, No. e2003066.
- (3) Sjoelander, S.; Urbaniczky, C. Integrated Fluid Handling System for Biomolecular Interaction Analysis. *Anal. Chem.* **1991**, *63*, 2338–2345.
- (4) Jacobus, C. J.; Chien, R. T. Two New Edge Detectors. *IEEE Trans. Pattern Anal. Mach. Intell.* **1981**, *PAMI-3*, 581–592.
- (5) Nenninger, G. G.; Piliarik, M.; Homola, J. Data Analysis for Optical Sensors Based on Spectroscopy of Surface Plasmons. *Meas. Sci. Technol.* **2002**, *13*, 2038–2046.
- (6) Thirstrup, C.; Zong, W. Data Analysis for Surface Plasmon Resonance Sensors Using Dynamic Baseline Algorithm. *Sens. Actuators, B* **2005**, *106*, 796–802.
- (7) Chinowsky, T. M.; Jung, L. S.; Yee, S. S. Optimal Linear Data Analysis for Surface Plasmon Resonance Biosensors. *Sens. Actuators, B* **1999**, *54*, 89–97.
- (8) Johnston, K. S.; Yee, S. S.; Booksh, K. S. Calibration of Surface Plasmon Resonance Refractometers Using Locally Weighted Parametric Regression. *Anal. Chem.* **1997**, *69*, 1844–1851.
- (9) Karabchevsky, A.; Karabchevsky, S.; Abdulhalim, I. Fast Surface Plasmon Resonance Imaging Sensor Using Radon Transform. *Sens. Actuators, B* **2011**, *155*, 361–365.
- (10) Zhou, A.; Chen, Y. Q. Fractional Order Processing of Quartz Crystal Microbalance Based DNA Biosensor Signals. *IFAC Proc. Vol.* **2006**, *39*, 188–193.
- (11) Chang, S. C.; Chao, I. J.; Liu, B. D.; Huang, C. Y.; Lee, M. H.; Lin, H. Y. Design of a Signal Processing Circuit for Quartz Crystal Microbalance Biosensors. In *Proceedings of International Conference on ASIC*; IEEE, 2011, pp. 180–183. DOI: 10.1109/ASICON.2011.6157151.
- (12) Songkhla, S. N.; Nakamoto, T. Signal Processing of Vector Network Analyzer Measurement for Quartz Crystal Microbalance with Viscous Damping. *IEEE Sens. J.* **2019**, *19*, 10386–10392.
- (13) Su, J.; Goldberg, A. F. G.; Stoltz, B. M. Label-Free Detection of Single Nanoparticles and Biological Molecules Using Microtoroid Optical Resonators. *Light Sci. Appl.* **2016**, *5*, No. e16001.
- (14) Pien, H. P.; Karl, W. C.; Puff, D.; Li, P.; Cunningham, B. Method and Apparatus for Biosensor Spectral Shift Detection. US718440B2, 2007.
- (15) Sailor, M. J. *Porous Silicon in Practice: Preparation, Characterization and Applications*; 1st Edition, Wiley-VCH: Weinheim, 2011. DOI: 10.1002/9783527641901.
- (16) Nguyen, H.; Park, J.; Kang, S.; Kim, M. Surface Plasmon Resonance: A Versatile Technique for Biosensor Applications. *Sensors* **2015**, *15*, 10481–10510.
- (17) Arshavsky-Graham, S.; Massad-Ivanir, N.; Segal, E.; Weiss, S. Porous Silicon-Based Photonic Biosensors: Current Status and Emerging Applications. *Anal. Chem.* **2019**, *91*, 441–467.
- (18) Moretta, R.; De Stefano, L.; Terracciano, M.; Rea, I. Porous Silicon Optical Devices: Recent Advances in Biosensing Applications. *Sensors* **2021**, *21*, 1336.
- (19) Zhao, Y.; Gaur, G.; Retterer, S. T.; Laibinis, P. E.; Weiss, S. M. Flow-through Porous Silicon Membranes for Real-Time Label-Free Biosensing. *Anal. Chem.* **2016**, *88*, 10940–10948.
- (20) Arshavsky-Graham, S.; Boyko, E.; Salama, R.; Segal, E. Mass Transfer Limitations of Porous Silicon-Based Biosensors for Protein Detection. *ACS Sens.* **2020**, *5*, 3058–3069.
- (21) Martín-Sánchez, D.; Ponce-Alcántara, S.; García-Rupérez, J. Sensitivity Comparison of a Self-Standing Porous Silicon Membrane under Flow-Through and Flow-Over Conditions. *IEEE Sens. J.* **2019**, *19*, 3276–3281.
- (22) Pacholski, C.; Sartor, M.; Sailor, M. J.; Cunin, F.; Miskelly, G. M. Biosensing Using Porous Silicon Double-Layer Interferometers: Reflective Interferometric Fourier Transform Spectroscopy. *J. Am. Chem. Soc.* **2005**, *127*, 11636–11645.
- (23) Mariani, S.; Pino, L.; Strambini, L. M.; Tedeschi, L.; Barillaro, G. 10 000-Fold Improvement in Protein Detection Using Nanostructured Porous Silicon Interferometric Aptasensors. *ACS Sens.* **2016**, *1*, 1471–1479.
- (24) Mariani, S.; Strambini, L. M.; Barillaro, G. Femtomole Detection of Proteins Using a Label-Free Nanostructured Porous Silicon Interferometer for Perspective Ultrasensitive Biosensing. *Anal. Chem.* **2016**, *88*, 8502–8509.
- (25) Pacholski, C. Photonic Crystal Sensors Based on Porous Silicon. *Sensors* **2013**, *13*, 4694–4713.
- (26) Schiff, S. J.; Aldroubi, A.; Unser, M.; Sato, S. Fast Wavelet Transformation of EEG. *Electroencephalogr. Clin. Neurophysiol.* **1994**, *91*, 442–455.
- (27) Goupillaud, P.; Grossmann, A.; Morlet, J. Cycle-Octave and Related Transforms in Seismic Signal Analysis. *Geoexploration* **1984**, *23*, 85–102.
- (28) Hecht, E. *Optics*; 5th ed.; Pearson: Essex, 2017.
- (29) Sundararajan, D. *Discrete Wavelet Transform : A Signal Processing Approach*; 1st ed.; Wiley: Hoboken, NJ, 2015.
- (30) Weiss Group. *Morlet Wavelet Phase Application*. <https://my.vanderbilt.edu/vuphotonics/resources>, <https://weissgroupvanderbilt.github.io/MorletWaveletPhaseApp/>, “Morlet Wavelet Phase” - MATLAB File Exchange: Vanderbilt University, Nashville, 2021.
- (31) Ellison, S. L. R.; Barwick, V. J.; Farrant, T. J. D. *Practical Statistics for the Analytical Scientist*; 2nd ed.; RSC: Cambridge, 2009, DOI: 10.1039/9781847559555.
- (32) Xifré-Pérez, E.; Ferré-Borrull, J.; Pallarés, J.; Marsal, L. F. Methods, Properties and Applications of Porous Silicon. In *Electrochemically Engineered Nanoporous Materials*; Losic, D.; Santos, A., Eds.; Springer: Cham, 2015, pp. 37–63. DOI: 10.1007/978-3-319-20346-1_2.
- (33) Wu, J.; Wang, C.; Li, X.; Song, Y.; Wang, W.; Li, C.; Hu, J.; Zhu, Z.; Li, J.; Zhang, W.; Lu, Z.; Yang, C. J. Identification, Characterization and Application of a G-Quadruplex Structured DNA Aptamer against Cancer Biomarker Protein Anterior Gradient Homolog 2. *PLoS One* **2012**, *7*, No. e46393.
- (34) Janshoff, A.; Dancil, K.-P. S.; Steinem, C.; Greiner, D. P.; Lin, V. S.-Y.; Gurtner, C.; Motesharei, K.; Sailor, M. J.; Ghadiri, M. R. Macroporous P-Type Silicon Fabry - Perot Layers . Fabrication , Characterization , and Applications in Biosensing. *J. Am. Chem. Soc.* **1998**, *12108*–12116.
- (35) Urmann, K.; Walter, J. G.; Scheper, T.; Segal, E. Label-Free Optical Biosensors Based on Aptamer-Functionalized Porous Silicon Scaffolds. *Anal. Chem.* **2015**, *87*, 1999–2006.
- (36) Tenenbaum, E.; Ben-Dov, N.; Segal, E. Tethered Lipid Bilayers within Porous Si Nanostructures: A Platform for (Optical) Real-Time Monitoring of Membrane-Associated Processes. *Langmuir* **2015**, *31*, 5244–5251.
- (37) Urmann, K.; Reich, P.; Walter, J. G.; Beckmann, D.; Segal, E.; Scheper, T. Rapid and Label-Free Detection of Protein a by Aptamer-Tethered Porous Silicon Nanostructures. *J. Biotechnol.* **2017**, *257*, 171–177.
- (38) Ukil, A.; Bärlocher, A. Implementation of Discrete Wavelet Transform for Embedded Applications Using TMS320VC5510. In

2007 *Symposium on Industrial Embedded Systems Proceedings*; IEEE, 2007, 357–360, DOI: [10.1109/SIES.2007.4297361](https://doi.org/10.1109/SIES.2007.4297361).

(39) Al-Ghouti, M. A.; Da'ana, D. A. Guidelines for the Use and Interpretation of Adsorption Isotherm Models: A Review. *J. Hazard. Mater.* **2020**, *393*, 122383.

(40) *The IUPAC Compendium of Chemical Terminology*; Gold, V., Ed.; International Union of Pure and Applied Chemistry (IUPAC): Research Triangle Park, NC, 2019, DOI: [10.1351/goldbook](https://doi.org/10.1351/goldbook).